Enhancement of optical and mechanical properties of Si nanopillars by ALD TiO$_2$ coating†

M. Pavlenko,[ab] E. L. Coy,[a] M. Jancelewicz,[a] K. Załęski,[a] V. Smyntyna,[b] S. Jurga[a] and I. Iatsunskyi*[a]

The mechanical and optical properties of Si and TiO$_2$–Si nanopillars (NPl) were investigated. Mesoporous silicon NPl arrays were fabricated by metal-assisted chemical etching and nanosphere lithography, and then pillars were covered by TiO$_2$ using the atomic layer deposition technique. We performed scanning electron microscopy (SEM), transmission electron microscopy (TEM), X-ray diffraction (XRD), energy dispersive X-ray spectroscopy (EDX), Raman spectroscopy, reflectance, photoluminescence (PL) spectroscopy and nanoindentation to characterize the as-prepared and annealed TiO$_2$–Si NPl. The main structural and mechanical parameters of TiO$_2$–Si NPl (grain size, strain, critical load, elastic recovery and Young's module) were calculated. Reflectance and PL spectroscopy were used to study the impact of morphology on optical properties of TiO$_2$–Si NPl before and after annealing. It was established that the nanostructures of TiO$_2$ penetrated inside the porous matrix of Si pillar improve the mechanical properties of TiO$_2$–Si NPl. The results of nanoindentation study have shown that Young's modulus of annealed TiO$_2$–Si NPl is about three times higher than for the pure Si NPl.

Introduction

Si nanopillars (NPl) are of great interest due to their potential applications in photovoltaics,[1–3] electronics,[4,5] sensors and biosensors,[6–8] and nanocapacitor arrays.[9] It has been demonstrated that Si NPl have several advantages over other silicon nanostructures such as enhanced light absorption,[3,10] efficient carrier transport,[11] superhydrophobicity,[12] strong carrier confinement,[13] and possibility to tune electronic and optical properties.[14] However, because of poor chemical stability and a high valence band maximum energy of Si comparing to hydrogen potential, it is difficult to simply use Si NPl in (photo) electrochemical applications. Therefore, nanocomposite structures based on Si NPl and metal oxides (*e.g.* Al$_2$O$_3$, TiO$_2$, ZnO) have been proposed to eliminate these shortcomings.

It has been shown that nanocomposite materials based on porous Si (PSi), Si nanowires (SiNW) and Si NPl could demonstrate unique properties, not observed in other nanosilicon structures. Recent publications show that nanocomposites based on nanostructured Si and TiO$_2$ possess enhanced photocatalytic activity due to their fast photogenerated charge carrier separation, low reflectance and high surface area.[15,16] Another broad area of applications of such nanocomposites is

(bio)sensors.[17,18] Authors have shown that combination of metal oxide nanostructures and PSi matrix, with well-defined structural properties gives a good possibility to enhance the sensor signal and sensitivity of the sensor/biosensor through tailoring structural properties of nanocomposites which is one of the main and actual problems in the field of sensors and biosensors.

Thus, the fabrication of Si NPl nanocomposites, as well as the study of their physical/chemical and structural properties will explore a development of new functional materials with high surface area and advanced properties for applications in bio-photonics, nanoelectronics or (photo)catalysis. It is also worth to mention, the optical and mechanical properties of Si NPl nanocomposites are closely related to their morphology. Therefore, a thorough study on the effect of morphology on the optical and mechanical properties of TiO$_2$–Si NPl is missing and further studies are still required.

A simple method to produce highly ordered Si NPl based on metal-assisted chemical etching (MACE) and nanosphere lithography, enabling control of the diameter, length and density of NPl arrays has been developed.[19,20] This approach allows controlling of the type, level, crystallographic orientation of dopant, and the orientation of Si NPl relative to the Si substrate. There is a number of methods to create nanocomposites of Si NPl. But as it was shown in recent researches, the most preferable method is Atomic Layer Deposition (ALD) technique.[21,22] It does not depend on substrate geometry and can be applied both for planar samples, 3D patterned substrates and porous media.[23,24] This method allows controlling the

[a] *NanoBioMedical Centre, Adam Mickiewicz University in Poznan, Umultowska 85, 61-614, Poznan, Poland. E-mail: yatsunskiy@gmail.com; igoyat@amu.edu.pl*

[b] *Department of Experimental Physics, Odessa I.I. Mechnikov National University, Pastera 42, 65026, Odessa, Ukraine*

thickness of nanolayers or size of nanocrystallites inside the PSi and the chemical composition by controlling the ALD parameters.

In this work, we report the effect of morphology on the optical and mechanical properties of the TiO_2–porous Si NPl composite system. To fabricate porous Si NPl, in this present study we used MACE and nanosphere lithography technique. Then Si NPl were covered by the TiO_2 using ALD. The morphology and phase composition of fabricated TiO_2–porous Si NPl were studied by the scanning and transmission electron microscopy (SEM, TEM), XRD, energy dispersive X-ray spectroscopy (EDX) and Raman spectroscopy. Optical properties have been analysed by means of reflectance and photoluminescence (PL) spectroscopy. Structural, optical, and mechanical parameters of TiO_2–porous Si NPl were estimated, and the correlation between them will be discussed. The mechanisms of the PL emissions will be proposed. The structural and optical changes induced by annealing will be discussed as well.

Experimental

Fabrication of Si nanopillars covered by ALD TiO2

Ordered arrays of Si ($\rho < 0.005\ \Omega$ cm resistivity, polished on the (100) face, B-doped) NPl with hexagonal symmetry were fabricated by combination of nanosphere lithography technique and MACE. Silicon samples ($1 \times 1\ cm^2$) were first cleaned by ethanol, acetone, and then by heating in a RCA solution (an aqueous mixture of 30% hydrogen peroxide (H_2O_2), 30% ammonium hydroxide (NH_4OH), and DI water with the volume ratio of $1:1:5$ at 80 °C for an hour, followed by a thorough rinse with DI water and drying in a stream of nitrogen (N_2). Polystyrene nanosphere 10% solution (mean diameter 600 nm) was mixed with an equal amount of ethanol and then applied to the deposition of a monolayer mask on a clean silicon surface by floating technique.[3] After deposition the size of nanosphere was decreased to approximately 300 nm using reactive ion etching (RIE) (MicroSys 200) in oxygen plasma. Following parameters were used: RF power – 70 W, and pressure – 0.6 mbar. A 120 nm Au film was deposited, as a catalyst, by magnetron sputtering machine (Quorum Q160T) in Ar atmosphere (50 mA, pressure 10^{-2} mbar). Then, the samples were etched in aqueous solution containing HF (40%), H_2O_2 (30%), and ultrapure H_2O at a ratio of $80:80:20\ H_2O_2/H_2O/HF$ for 15 min. The Au film was removed using a solution of Aqua Regia (HCl (35%) and HNO_3 (65%) at ratio $1:2$) and then samples were dipped in HF (5%) solution for 3 min to remove native oxide. After all procedures samples of Si NPl were cleaned with deionized water and blown dry with N_2.

The ALD TiO_2 was deposited onto the samples of Si NPl using $TiCl_4$ and water as ALD precursors. The ALD cycle consisted of 0.3 s exposure to $TiCl_4$, 4 s N_2 purge, 0.3 s exposure to water and 4 s N_2 purge. The temperature of ALD was 200 °C. The number of deposition–purge cycles was 500 corresponding to approximately 20 nm of the TiO_2 film on the planar silicon surface. The growth rate was typically 0.4 Å per cycle for TiO_2 on the planar silicon surface. After TiO_2 deposition some samples were annealed at 450 °C for an hour in an ambient atmosphere.

Characterization

Structural and chemical compositions of NPl were analysed by transmission (JEOL ARM 200F) and scanning (JEOL, JSM-7001F) electron microscopy (TEM/SEM). The lamellas for TEM were prepared by focused ion beam (FIB-JEOL JIB-4000) by the method described in ref. 25. GIXRD measurements were performed on X'pert3 MRD (XL) from PANalytical, working with a Cu Kα radiation source (wavelength of 1.54 Å) and operating at 45 kV and 40 mA. Raman scattering measurements were performed using a Renishaw micro-Raman spectrometer equipped with a confocal microscope (Leica). The Raman scattering spectra were excited by a 514 nm laser. The beam was focused on the samples with a 50× microscope objective with a numerical aperture of 0.4. Optical properties of TiO_2–Si NPl have been studied with reflectance (UV-vis spectrophotometer lambda 950 UV/vis/NIR range 300–1100 nm, 1 nm step) and photoluminescence spectroscopy (PL). PL of the samples was measured at room temperatures using a home-made setup. The excitation of PL was performed with a nitrogen laser (337.7 nm). Finally, mechanical properties of the samples were investigated by nanoindentation (Hysitron TI 950 TriboIndenter) using a Berkovich diamond indenter at maximum load of 40 μN.

Results and discussion

In order to examine the morphology of pristine Si NPl, and NPl after TiO_2 ALD, SEM and TEM characterizations were carried out. Fig. 1(a) shows the typical large-scale SEM image of the formed Si NPl. Non-uniform distribution of NPl arrays is a result of the way the polystyrene spheres are float-transferred onto the Si substrate. Nevertheless, relatively large areas, up to 10 μm, are covered with the uniform hexagonal pillar arrays.

The cross-sectional TEM image of Si NPl is presented in the Fig. 1(b). The distance between two adjacent pillars is approximately 0.7 μm, the diameter and the height are 0.4 and 1.5 μm, respectively. Geometrical parameters of fabricated NPl could be controlled by varying the MACE and nanosphere lithography procedures. The outer surface of NPl is rough and porous. The roughness of the Si NPl is due to the roughness in the outer edge of polystyrene spheres (Fig. S1†). The porosity can be observed more clearly in the high-magnification SEM and TEM images of the NPl (Fig. 1(c–e)). Pillars have a mesoporous structure with an average pore size less than 10 nm. Below Si NPl a mesoporous layer of 1.5 μm thick can be also observed. Bechelany *et al.* proposed one of the possible mechanism responsible for sidewall etching.[26] They have shown that gold assisted chemical etching (vertical etching) is in competition with chemical isotropic etching (sidewall etching) of the bulk Si enhanced by its high dopant concentration. After 500 cycles of ALD a conformal TiO_2 layer on the Si NPl was obtained (Fig. 1(f)). It is difficult to identify any individual grains of the TiO_2 (Fig. S2†). TEM results show that the porous inside the Si NPl are filled by TiO_2 (Fig. S3†).
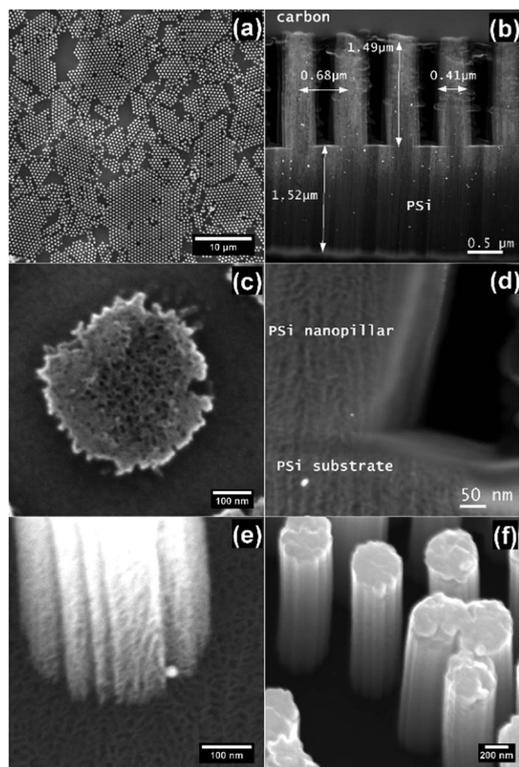
Fig. 1 Si and TiO$_2$−Si NPl arrays, (a) plane view SEM image of pristine Si NPl, (b) cross-sectional TEM image of Si NPl, (c) the top surface of the pillar, (d) cross-sectional HRTEM image of Si NPl, (e) high resolution SEM image of the pillar, (f) SEM image of TiO$_2$−Si NPl.

In addition, we have studied the elemental distribution over the NPl using EDX mapping. As can be seen in Fig. 2, both titanium (magenta) and oxygen (green) elements are distributed quite uniformly inside the Si NPl for as-deposited samples. One can also observe oxygen and titanium penetrating the PSi layer beneath the pillar. In the case of porous structures, during the
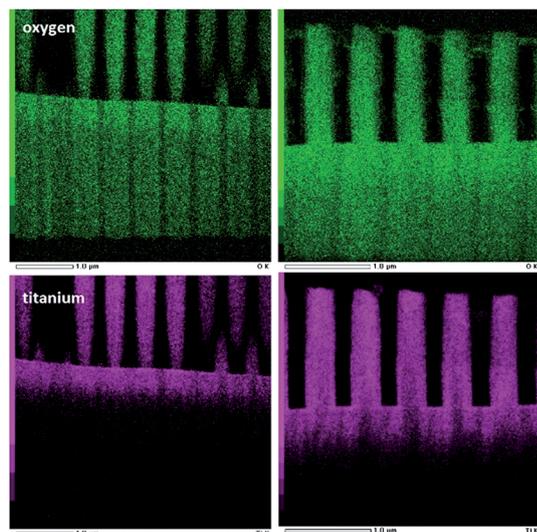
ALD process, molecules of precursors penetrate into the pore, and forming nanostructures of TiO$_2$ inside the porous matrix of Si NPl as well as the bottom PSi layer. The elemental distribution of titanium atoms remains almost the same after the annealing. However, we observed the increasing of oxygen concentration in the Si NPl and PSi layer indicating on enhanced oxidation of the Si during the annealing (Fig. S4†).

Fig. 3 shows the GIXRD of Si NPl covered with TiO$_2$ layer after 500 ALD cycles. For Si NPl we can see the most intensive Si peak located at 55.78° and corresponding to (311) orientation.[27] Titanium ALD deposition leads to the substantial X-ray scattering and considerable intensity decreasing. We do not observe XRD peaks corresponding to crystalline titanium phase. Thus, we can conclude that after ALD, titanium dioxide is mainly in an amorphous or highly polycrystalline phase what was also confirmed by TEM and Raman spectroscopy (shown later). After annealing, one can notice XRD peaks centred at 25.27°, 37.8°, 48.02° and 62,45° corresponding to (101), (004), (200) and (200) of TiO$_2$ anatase phase (JCPDS 21-1272), respectively. It might be explained by the amorphous-to-crystalline phase transition occurring in the TiO$_2$ during annealing.[23]

It is well known that XRD peak analysis is a powerful and simple method to estimate the nanocrystallites size and the lattice strain.[28,29] The average size of TiO$_2$ nanocrystallites can be determined using the Scherer equation:[30]

$$D = \frac{0.94\lambda}{\text{FWHM} \cos(\theta)}, \tag{1}$$

where D is the average size of nanocrystallites, λ – the X-ray wavelength, FWHM – full width at half maximum of the XRD peaks centered at θ degree.

The strain-induced broadening in TiO$_2$ and Si nanocrystallites was calculated using the formula:[31]

$$\varepsilon = \frac{\text{FWHM}}{4tg(\theta)}. \tag{2}$$

Because of the total peak broadening is represented by the sum of the contributions of strain and crystallite size, the

Fig. 2 EDX element mapping images of the TiO$_2$-NPl before (left images) and after annealing (right images).
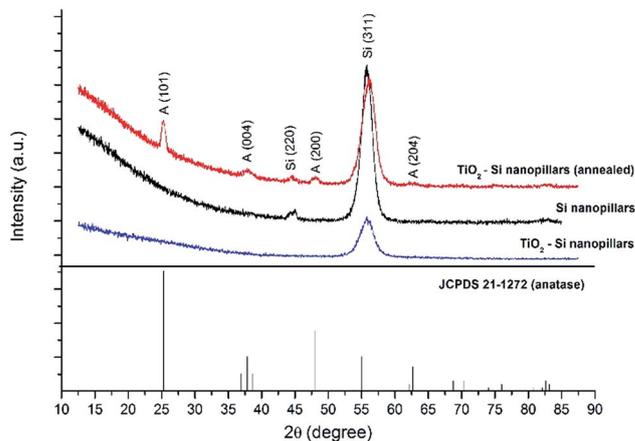

Fig. 3 GIXRD of Si NPl before and after ALD deposition with JCPDS (21-1272) data of anatase.

Williamson–Hall approach should be applied to determine the main broadening factor.[32,33] However, in order to apply the Williamson–Hall approach correctly, more XRD peaks should be considered in calculations.[32,33] In our case it was not applicable. Therefore, we have estimated the strain and crystallite size separately, using formula (1) and (2).

Calculated values of the average size of TiO$_2$ and Si nanocrystallites, and strains are presented in the Table 1. It is clearly seen, the average size of Si nanocrystallites remains almost the same after deposition and annealing. On the other hand, we can notice that the value of the strain in Si increases for as-deposited samples and takes the initial value ($\varepsilon = 0.0149$) after annealing. This may be explained by considering that ALD TiO$_2$ penetrating inside the pores of Si NPl generates additional deformations, and thus increasing the strain value of silicon. With the annealing, the amorphous TiO$_2$ coalesces to form a continuous film of the anatase nanograins reducing the value of the strain. The increase in average crystallite size of anatase indicates an increase in the crystallinity of TiO$_2$.

In order to determine the phase of obtained materials we also used μ-Raman spectroscopy as very sensitive local method. Raman spectra for Si and TiO$_2$–Si NPl are presented in Fig. 4. An intensive asymmetric, red-shifted peak at about 510 cm^{-1} corresponds to phonon mode of nanosilicon.[34] The position and the shape of this peak indicate the presence of nanocrystalline and/or amorphous phase of the Si.[35] No peak from the c-Si substrate was seen in any of the Raman spectra. A broad peak between 900 and 1100 cm^{-1} is related to few transverse optical phonons of PSi.[36]

In addition to nanostructured silicon studying, Raman spectroscopy was also used to detect and identify TiO$_2$. The first intensive peak of TiO$_2$ is located at about 150 cm^{-1} and attributed to E$_g$ mode. This is typical of the anatase TiO$_2$ phase, however the peak is broader and blue-shifted with respect to bulk anatase (peak position is 144 cm^{-1} and FWHM is 7 cm^{-1}).[30] Other Raman peaks at 200, 397 and 634 cm^{-1} are also attributed to the anatase phase for E$_g$ and B$_{1g}$ modes, respectively.[37,38] After annealing the intensity of all anatase peaks increases, indicating increased crystallinity of TiO$_2$. The broadening and blue-shift of the anatase Raman peak are attributed to phonon confinement effects that usually exist in nanomaterials.[30] In order to calculate the average size of anatase
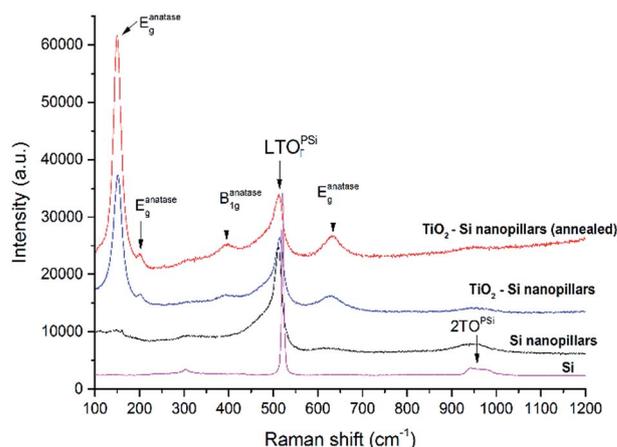

Fig. 4 Raman spectra of Si NPl before and after ALD deposition with the Raman spectrum of c-Si shown for comparison.

and silicon nanocrystallites we used a simple confinement model described in our previous publications.[30,36] In this model the first-order Raman spectrum $I(\omega)$ for spherical nanocrystals is given by:

$$I(\omega) = \int_{BZ} \frac{4\pi q^2 \exp\left(-\dfrac{q^2 L^2}{16\pi^2}\right) \mathrm{d}^3 q}{\left(\omega - \omega(q)\right)^2 - \left(\dfrac{\Gamma_0}{2}\right)^2}, \tag{3}$$

where Γ_0 is the Raman linewidth at room temperature, and $\omega(q)$ is the phonon dispersion curve (for anatase – $\omega = \omega_0 + \Delta[1 - \cos(qa)]$,[30] and for silicon – $\omega = A - Bq^2$,[35] ω_0 – maximum peak position, $\Delta = 20$ cm^{-1}, $a = 0.3768$ nm, A and B – constants). The average size of anatase and silicon nanocrystallites was estimated and results are presented in the Table 1 (Fig. S5†). It is seen that the average crystallite size calculated form XRD and Raman spectroscopy differ by several nanometers. Taking into account that the penetration depth (PD) of the laser spot in the Raman spectroscopy differs from the X-ray beam PD, we can conclude that there is some distribution of the average crystallite size along the pillars and surface.

However, Khorasaninejad et al. showed that if confinement effects take place in nanosilicon, the red-shifting would be

Table 1 Structural and mechanical parameters of TiO$_2$–Si NPl

Samples		Si NPl	TiO$_2$–Si NPl		TiO$_2$–Si NPl (annealed)	
Material		Si	Si	Anatase	Si	Anatase
XRD	Peak pos. [degree]	55.78	56.05	—	55.79	25.27
	FWHM [degree]	1.57	2.29	—	1.89	0.65
	D [nm]	5.89 ± 0.3	4.09 ± 0.6	—	4.95 ± 0.45	13.0 ± 0.4
	ε	0.0149	0.0189	—	0.0150	0.0127
Raman	Peak pos. [cm^{-1}]	511.1	512.2	149.8	514	150.8
	FWHM [cm^{-1}]	16.48	19.77	21.7	18.2	18.8
	D [nm]	8.1 ± 0.3	7.7 ± 0.3	7.3 ± 0.2	7.8 ± 0.3	11.6 ± 0.2
	ε	0.0107	0.0129	—	0.0118	—

approximately $1–2$ cm^{-1}.[39] In other cases, the compressive stress and defects affect mainly on the red-shifting. We calculated the value of the strain effect using following equation:[40]

$$\frac{\delta\omega}{\omega} = -3\gamma\varepsilon, \qquad (4)$$

where $\delta\omega$ is the peak width, and $\gamma = 1$ is the Gruneisen constant. Comparing strains calculated from XRD and Raman spectra, one can notice a slight difference in these values. However, the tendency, to increase the strain in nanosilicon after ALD and to reduce it after annealing, remains the same.

Fig. 5(a) shows the absolute reflectance of fabricated Si and TiO$_2$–Si NPl at $8°$ incidence over the range of 200–1100 nm. The optical reflectivity for Si NPl decreases significantly comparing to polish Si surface, which is consistent with the results reported previously.[41,42] One can observe that the reflectivity of Si NPl decreases to approximately 2% throughout the entire range of wavelengths from 200 nm to 1100 nm, without any anti-reflection coatings. It might be explained by the existence of the porous structures of NPl, which induce the enhanced scattering and light absorption. The total reflectivity for the TiO$_2$–Si NPl increases a few percent. While the reflectivity for annealed TiO$_2$–Si NPl decreases and remains in the same order as the reflectivity of pristine Si NPl. This effect could be explained by

(a)

(b)

Fig. 5 (a) Absolute optical reflectance and (b) PL spectra from the Si and TiO$_2$–Si NP arrays.

the change of refractive index due to pores filling and further crystallization of TiO$_2$.[30]

The PL of Si and TiO$_2$–Si NPl were measured in the region of light wavelengths from 400 to 850 nm (Fig. 5(b)). The maximum of the PL peak for pristine Si NPl was detected at 665 ± 5 nm (1.87 eV), which revealed the good quality of the nanostructured Si. This red emission from PSi NPl is mainly due to the quantum confinement in Si nanocrystallites.[43] After ALD deposition of TiO$_2$, the PL spectra showed one broad peak at approximately 450 ± 5 nm (2.75 eV). The PL band at 2.75 eV is attributed to oxygen vacancies with two electrons in the anatase.[44,45] However, after the deposition of TiO$_2$, the PL intensity is degraded because of a lower recombination rate. We can explain this by the enhanced separation of the photogenerated charge carriers due to a difference in the energy levels of their conduction and valence bands.[36] Previously, we have shown that two types of defects (volume and surface) affect on the PL of the TiO$_2$ inside the PSi.[30] PL relating to volume defects (oxygen vacancies) should be crucial for TiO$_2$ with a low concentration of surface defects, which is typical for high crystalline quality materials. Thus, after annealing, the crystallinity becomes very high, and we can observe the increasing of PL through oxygen vacancies in the TiO$_2$.

At this point, it is clear that the porous nature of the NPl allows the inclusion of TiO$_2$ increasing the internal strain of the pillars and, perhaps, reinforcing its structural properties. The nanomechanical properties of the pillars are investigated using nanoindentation. Previous studies have shown that the porosity of Si has a direct correlation with its elastic constant,[46] thus by proving the elastic response of pure NPl, the Young's modulus can be extracted by the Oliver–Pharr method and the overall porosity of the pillars estimated.[47]

Pillars were tested by scanning a small region of the surface (4×4 μm) and performing low compression tests on specific pillars. Load *vs.* displacement curves are presented in Fig. 6 and extracted data in the Table 2. Young's modulus of pure silicon pillars corresponds to relative density of 0.2%, or an overall porosity of 70–80%,[48] furthermore the general behavior of the NPl follows that of a super elastic material, with total recovery above 90%, extracted from the ratio between maximum load (H_{max}) and contact depth (H_c). Interestingly enough, Si–TiO$_2$ NPl show a clear plasto-elastic response, observed in the unload section of the curve, this response is compatible with both, the elastic response of the pillar and the highly plastic deformation of amorphous TiO$_2$ inside the NPl. The annealing of the structures shows the clear improvement on crystallinity of the anatase phase (Fig. 3), which, as shown in Fig. 6(a), dramatically increases the Young modulus of the pillars. This improvement is associated with the nanocrystalline particles confined in the porous after their crystallization, NPl would behave as nanocomposite like structure in which the Si confinement will bring the structural stability, while the nanocrystals provide the fracture resistance and improved Young's modulus observed,[49] behaviour previously observed in amorphous,[50] and amorphous-to-crystalline structured nanolaminates.[51]

Another important parameter evaluated by nanoindentation is the critical load (P_{crit}), which can be understood as the
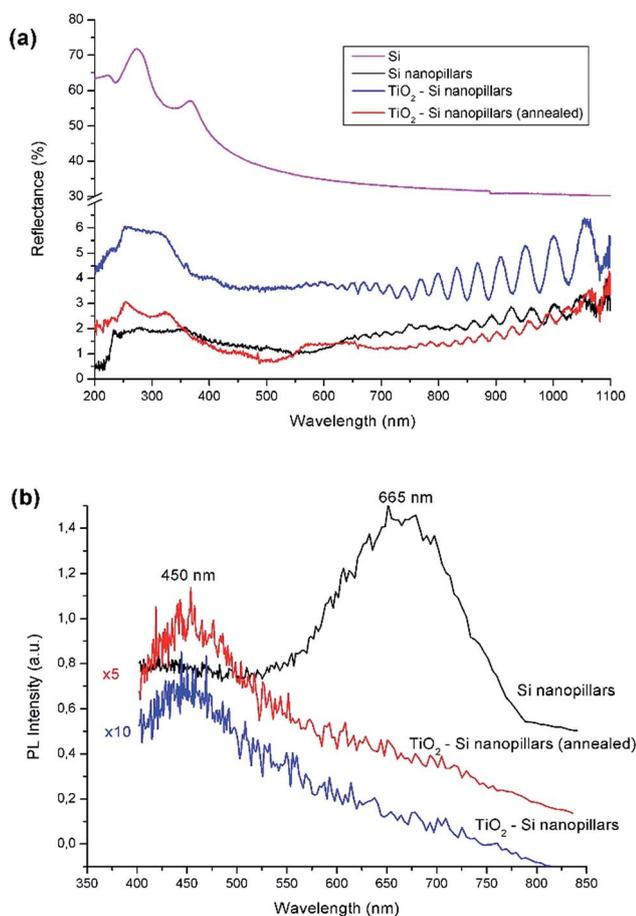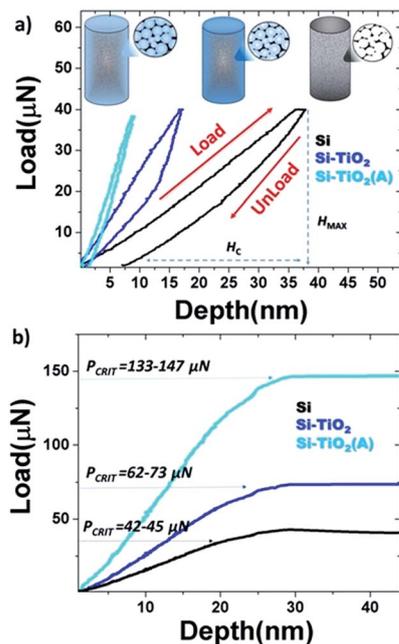
Fig. 6 Nanoindentation curves (load *vs.* displacement) for nanopillars of Si, Si–TiO$_2$ and Si–TiO$_2$ (A-annealed).

Table 2 Mechanical parameters of TiO$_2$–Si NPl obtained from nanoindentation

Samples	Si NPl	TiO$_2$–Si NPl	TiO$_2$–Si NPl (annealed)
Young's modulus [GPa]	6.1 ± 0.5	8.7 ± 0.5	18.4 ± 1.5
Elastic recovery (%)	81	93	95
Critical load [μN]	42–45	62–73	133–147

fracture and collapse of the pillars under uniaxial pressure Fig. 6(b). The critical load values show the monotonic increment of the pillars resilience with the inclusion of TiO$_2$ inside the porous and its highest values after the annealing of the samples (Table 2). The critical loads found are compatible with those of monocrystalline nanowires of ZnO reported in the literature,[52] although the measured Young's modulus is much lower, the critical load is not. This shows the important enhancement of the mechanical properties of the Si NPl with the inclusion of TiO$_2$ and posterior annealing.

Conclusions

In summary, TiO$_2$–porous Si NPl were fabricated using MACE and ALD. The morphology, optical and mechanical properties of TiO$_2$–porous Si nanopillars were studied, and the main structural and mechanical parameters were estimated. The average value of strains and the approximate size of Si and TiO$_2$ nanocrystals were estimated using XRD and Raman spectroscopy. It was established that optical and mechanical properties of TiO$_2$–Si NPl are tailored by their morphology. The quenching of the PL emission and optical reflectance decreasing were discussed relatively to morphology of TiO$_2$–Si NPl. It was shown that the inclusion of TiO$_2$ in the porous matrix of Si improve the mechanical properties of TiO$_2$–Si NPl. The results obtained in this research are very promising for the improved use of Si NPl covered by TiO$_2$ in photocatalysis and biosensors applications,[7,8] where it is important to have structures with a large effective surface area and fast charge carrier separation.

References

1 E. Kim, Y. Cho, A. Sohn, H. Hwang, Y. U. Lee, K. Kim, H.-H. Park, J. Kim, J. W. Wu and D.-W. Kim, *Sci. Rep.*, 2016, **6**, 29472.

2 J. Shieh, Y. C. Li, C. Y. Ji, C. C. Chiu and H. Y. Lin, *J. Renewable Sustainable Energy*, 2015, **7**, 033102.

3 F. Teng, N. Li, L. Liu, D. Xu, D. Xiao and N. Lu, *RSC Adv.*, 2016, **6**, 15803–15807.

4 T. Kirkpatrick, C. B. Simmons, A. J. Akey, N. Tabet and T. Buonassisi, *J. Appl. Phys.*, 2016, **119**, 194501.

5 E. Mills, J. Cannarella, Q. Zhang, S. Bhadra, C. B. Arnold and S. Y. Chou, *J. Vac. Sci. Technol., B: Nanotechnol. Microelectron.: Mater., Process., Meas., Phenom.*, 2014, **32**, 06FG10.

6 H. S. Wasisto, S. Merzsch, A. Stranz, A. Waag, E. Uhde, T. Salthammer and E. Peiner, *Sens. Actuators, B*, 2013, **189**, 146–156.

7 B. D. Choudhury, R. Casquel, M. J. Bañuls, F. J. Sanza, M. F. Laguna, M. Holgado, R. Puchades, A. Maquieira, C. A. Barrios and S. Anand, *Opt. Mater. Express*, 2014, **4**, 1345–1354.

8 M. Kandziolka, J. J. Charlton, I. I. Kravchenko, J. a. Bradshaw, I. a. Merkulov, M. J. Sepaniak and N. V. Lavrik, *Anal. Chem.*, 2013, **85**, 9031–9038.

9 S. Chang, J. Oh, S. T. Boles and C. V Thompson, *Appl. Phys. Lett.*, 2010, **96**, 153108.

10 a. Smyrnakis, E. Almpanis, V. Constantoudis, N. Papanikolaou and E. Gogolides, *Nanotechnology*, 2015, **26**, 85301.

11 V. Gowrishankar, S. R. Scully, A. T. Chan, M. D. McGehee, Q. Wang and H. M. Branz, *J. Appl. Phys.*, 2008, **103**, 064511.

12 B. Kiraly, S. Yang and T. J. Huang, *Nanotechnology*, 2013, **24**, 245704.

13 X. Zhao, C. M. Wei, L. Yang and M. Y. Chou, *Phys. Rev. Lett.*, 2004, **92**, 236805.

14 R. Ghosh, P. K. Giri, K. Imakita and M. Fujii, *Nanotechnology*, 2014, **25**, 45703.

15 Y. J. Hwang, A. Boukai and P. Yang, *Nano Lett.*, 2009, **3**, 410–415.

16 S. Sampath, P. Maydannik, T. Ivanova, M. Shestakova, R. Nagumothu and V. Alagan, *Superlattices Microstruct.*, 2016, **97**, 155–166.

17 D. Yan, S. Li, S. Liu, M. Tan, D. Li and Y. Zhu, *J. Solid State Electrochem.*, 2016, **20**, 459–468.

18 J. Liao, Z. Li, G. Wang, C. Chen, S. Lv and M. Li, *Phys. Chem. Chem. Phys.*, 2016, **18**, 4835–4841.

19 S. Soleimani-Amiri, A. Gholizadeh, S. Rajabali, Z. Sanaee and S. Mohajerzadeh, *RSC Adv.*, 2014, **4**, 12701–12709.

20 H. Lin, M. Fang, H.-Y. Cheung, F. Xiu, S. Yip, C.-Y. Wong and J. C. Ho, *RSC Adv.*, 2014, **4**, 50081–50085.

21 Y. Yan, D. Wang and P. Schaaf, *Dalton Trans.*, 2014, **43**, 8480–8485.

22 B. Zhong, T. Zhang, X. X. Huang, G. W. Wen, J. W. Chen, C. J. Wang and Y. D. Huang, *Mater. Lett.*, 2015, **151**, 130–133.

23 I. Iatsunskyi, M. Jancelewicz, G. Nowaczyk, M. Kempiński, B. Peplińska, M. Jarek, K. Załęski, S. Jurga and V. Smyntyna, *Thin Solid Films*, 2015, **589**, 303–308.

24 R. Viter, I. Iatsunskyi, V. Fedorenko, S. Tumenas, Z. Balevicius, A. Ramanavicius, S. Balme, M. Kempin, G. Nowaczyk, S. Jurga and M. Bechelany, *J. Phys. Chem. C*, 2016, **120**, 5124–5132.

25 I. Iatsunskyi, E. Coy, R. Viter, G. Nowaczyk, M. Jancelewicz, I. Baleviciute, K. Załęski and S. Jurga, *J. Phys. Chem. C*, 2015, **119**, 20591–20599.

26 B. Mikhael, B. Elise, M. Xavier, S. Sebastian, M. Johann and P. Laetitia, *ACS Appl. Mater. Interfaces*, 2011, **3**, 3866–3873.

27 M. Kanayama, T. Oku, T. Akiyama, Y. Kanamori, S. Seo, J. Takami, Y. Ohnishi, Y. Ohtani and M. Murozono, *Energy Power Eng.*, 2013, **5**, 18–22.

28 K. Thamaphat, P. Limsuwan and B. Ngotawornchai, *Nat. Sci.*, 2008, **42**, 357–361.

29 A. Monshi, *World J. Nano Sci. Eng.*, 2012, **2**, 154–160.

30 I. Iatsunskyi, M. Pavlenko, R. Viter, M. Jancelewicz, G. Nowaczyk, I. Baleviciute, K. Załęski, S. Jurga, A. Ramanavicius and V. Smyntyna, *J. Phys. Chem. C*, 2015, **119**, 7164–7171.

31 C. Suryanarayana and M. G. Norton, *Microsc. Microanal.*, 1998, **4**, 513–515.

32 V. Mote, Y. Purushotham and B. Dole, *Journal of Theoretical and Applied Physics*, 2012, **6**, 6.

33 D. Arora, K. Asokan, A. Mahajan, H. Kaur and D. P. Singh, *RSC Adv.*, 2016, **6**, 78122–78131.

34 S. Piscanec, M. Cantoro, a. Ferrari, J. Zapien, Y. Lifshitz, S. Lee, S. Hofmann and J. Robertson, *Phys. Rev. B: Condens. Matter Mater. Phys.*, 2003, **68**, 2–5.

35 Z. Sui, P. P. Leong, I. P. Herman, G. S. Higashi and H. Temkin, *Appl. Phys. Lett.*, 1992, **60**, 2086–2088.

36 I. Iatsunskyi, G. Nowaczyk, S. Jurga, V. Fedorenko, M. Pavlenko and V. Smyntyna, *Optik*, 2015, **126**, 1650–1655.

37 I. A. Alhomoudi and G. Newaz, *Thin Solid Films*, 2009, **517**, 4372–4378.

38 A. Gajovi, M. Stubičar, M. Ivanda and K. Furi, *J. Mol. Struct.*, 2001, **563–564**, 315–320.

39 M. Khorasaninejad, M. M. Adachi, J. Walia, K. S. Karim and S. S. Saini, *Phys. Status Solidi*, 2013, **5**, 373–377.

40 T. Kamiya, M. Kishi, a. Ushirokawa and T. Katoda, *Appl. Phys. Lett.*, 1981, **38**, 377–379.

41 J.-W. Kang, Y.-J. Kang, S. Jung, M. Song, D.-G. Kim, C. S. Kim and S. H. Kim, *Sol. Energy Mater. Sol. Cells*, 2012, **103**, 76–79.

42 P. R. Pudasaini and A. a. Ayon, *Microelectron. Eng.*, 2013, **110**, 126–131.

43 J. Zi, K. Zhang and X. Xie, *Phys. Rev. B: Condens. Matter Mater. Phys.*, 1997, **55**, 9263–9266.

44 S. G. Yenchalwar, V. K. Azhagan and M. V. Shelke, *Phys. Chem. Chem. Phys.*, 2014, **16**, 17786–17791.

45 Y.-H. Chang, C.-M. Liu, C. Chen and H.-E. Cheng, *J. Electrochem. Soc.*, 2012, **159**, D401–D405.

46 D. Bellet, P. Lamagnère, A. Vincent and Y. Bréchet, *J. Appl. Phys.*, 1996, **80**, 3772.

47 W. C. Oliver and G. M. Pharr, *J. Mater. Res.*, 1992, 7, 1564–1583.

48 O. Dmitrieva, D. Raabe, S. Müller and P. W. Dondl, *Lecture Notes in Applied and Computational Mechanics*, 2015, **78**, 205–218.

49 D. Martínez-Martínez, in *Encyclopedia of Tribology*, ed. Q. J. Wang and Y.-W. Chung, Springer US, Boston, MA, 2013, pp. 2359–2364.

50 E. Coy, L. Yate, Z. Kabacińska, M. Jancelewicz, S. Jurga and I. Iatsunskyi, *Mater. Des.*, 2016, **111**, 584–591.

51 R. Raghavan, M. Bechelany, M. Parlinska, D. Frey, W. M. Mook, A. Beyer, J. Michler and I. Utke, *Appl. Phys. Lett.*, 2012, **100**, 191912.

52 E. Robak, E. Coy, M. Kotkowiak, S. Jurga, K. Załęski and H. Drozdowski, *Nanotechnology*, 2016, **27**, 175706.